Dilute granular flow around an immersed cylinder

C. R. Wassgren[a)] and J. A. Cordova
School of Mechanical Engineering, Purdue University, West Lafayette, Indiana 47907

R. Zenit
Instituto de Investigaciones en Materiales, Universidad Nacional Autónoma de México,
Apdo. Postal 70-360, Ciudad Universitaria, México D.F. 04510, México

A. Karion
Carderock Division, Naval Surface Warfare Center, 9500 MacArthur Boulevard, West Bethesda,
Maryland 20817

In this paper we investigate a two-dimensional dilute granular flow around an immersed cylinder using discrete element computer simulations. Simulation measurements of the drag force acting on the cylinder, F_d, are expressed in terms of a dimensionless drag coefficient, C_d $=F_d/[\frac{1}{2}\rho \nu_\infty U_\infty^2(D+d)]$, where ρ is the upstream particle mass density, ν_∞ is the upstream solid fraction, U_∞ is the upstream velocity, and $(D+d)$ is the sum of the cylinder diameter, D, and surrounding particle diameter, d. The drag coefficient increases rapidly with decreasing Mach number for subsonic Mach numbers, but remains insensitive to Mach number for supersonic values. The drag coefficient is also a strong function of the flow Knudsen number, with the drag coefficient increasing with increasing Knudsen number and approaching an asymptotic value for very large Knudsen numbers. The drag coefficient decreases with decreasing normal coefficient of restitution and is relatively insensitive to the friction coefficient. Bow shock structures and expansion fans are also observed in the simulations and are compared to similar structures observed in compressible gas flows. © *2003 American Institute of Physics.* [DOI: 10.1063/1.1608937]

I. INTRODUCTION

A granular material consists of an assembly of solid particles dispersed in a surrounding fluid or vacuum. In a granular flow, the momentum transport due to particle motion and particle–particle interactions is a significant component to the overall momentum transport. Granular flows are common in a number of industries including those that manufacture or process chemicals, pharmaceuticals, powdered ceramics, food stuffs, ores, and building materials. Granular flows are also observed in many natural processes such as avalanches, landslides, dune formation, and planetary ring formation.

Of particular interest in this paper is the flow of a granular material around an immersed object. Such flows are commonly observed in devices used to store, handle, or probe granular materials. For example:

(1) Agitating blades or bars are routinely used in mixing and granulating devices.[1]
(2) Inserts are often used as structural supports and flow deflection devices for reducing the dynamic stresses that occur during filling and emptying of grain bins.[2,3]
(3) Agricultural tilling and earth-moving construction equipment push or drag surfaces through granular soils.
(4) Impact probes have been used to determine soil characteristics.[4]
(5) Fluidized beds and chute flows often contain immersed pipes that serve as heat transfer surfaces.[5]

(6) Size segregation of particulate materials often involves the relative motion of a large immersed impurity in an otherwise homogeneous bed of surrounding particles.[6]

Having a better understanding of the flow dynamics in these and other applications is critical for improving particle handling and processing equipment. In particular, designers are interested in predicting the forces, wear, and flow patterns around immersed objects. Clearly, having a better understanding of the dynamics of an object immersed in a granular flow will have ramifications in a wide range of applications.

Background

Wieghardt[7] was one of the first to study granular flow around an immersed object. He performed a series of experiments in dense granular flows consisting of partially immersed rods dragged through beds of sand. A dense granular flow is defined as one in which momentum transfer between grains occurs primarily through long-lasting, multiple particle contacts. Wieghardt found that the drag on an immersed rod has a weak dependence on the translational velocity and cross-sectional shape of the rod, although there is a square-root dependence on the rod's projected diameter. He reasoned that the weak velocity dependence is due to the fact that the drag acting on the rod at slow velocities is caused by sliding friction interactions with the surrounding particles, a mechanism that is independent of velocity. Recently, Albert

---

a)Author to whom correspondence should be addressed.

et al.[8] revisited this problem but used much slower velocities, on the order of 1 mm/s rather than the 1–100 cm/s used by Wieghardt, and found similar results although they observed a linear dependence on the object's projected diameter rather than the square-root dependence observed by Wieghardt.

Atkinson *et al.*[9] also investigated the drag on objects immersed in a slow moving, dense granular flow. Their experiments focused primarily on the force on long surfaces oriented parallel to the flow in a vertical chute. They also found that the drag force is insensitive to the flow velocity and again attributed this to frictional interactions. Atkinson *et al.* compared their measurements with models based on Janssen's method of differential slices[10] and found reasonable agreement for very long surfaces in which the leading edge of the surface is not immersed in the flow. However, when the leading edge of the object is immersed in the flow, the model under-predicts the drag force by an order of magnitude. They attributed the large discrepancy to the formation of a stagnant zone and stress discontinuity upstream of the object, a feature similar to the bow shock that forms in front of a blunt object in a supersonic gas flow.[11]

Tüzün and Nedderman[2,12] studied the flow patterns around silo inserts and the wall stresses resulting from their presence. They conducted experiments in a dense, vertical channel flow with square and triangular obstacles. They found that stagnant zones of material form on the upstream side of the insert and a large void region forms downstream of the object. Similar observations have been made by Pearce and Sabersky[5] in their investigations of heat transfer from an immersed cylinder. Tüzün and Nedderman also found that "switch" stresses, a phenomenon associated with transition from an active to a passive failure state in a Mohr–Coulomb material,[10] occur in the surrounding material as a result of the inserts. Hernandez-Cordero *et al.*[3] also investigated the use of inserts in grain silos. They found that grain losses due to crushing are significantly reduced when inserts are used since the inserts carry most of dynamic stress during hopper discharge.

Recently Chehata *et al.*[13] investigated dense, frictional granular flow around a cylinder in a quasi-two-dimensional vertical chute. They observed stagnant and void regions similar to those reported by Tüzün and Nedderman[2,12] and Pearce and Sabersky.[5] In addition, Chehata *et al.* found that the drag coefficient for the cylinder decays inversely with the square of the flow Froude number based on the chute's hydraulic diameter. They also observed that the granular temperature and vorticity of the granular flow are non-zero only in the vicinity of the cylinder surface.

The drag force acting on a sphere dragged horizontally through a vibro-fluidized granular bed was investigated by Zik *et al.*[14] They found that the drag force acting on the sphere is proportional to the sphere's velocity; an observation in contrast to the previously discussed observations where the drag force is independent of the flow velocity. This discrepancy can be attributed to the fact that the surrounding granular material in the experiments of Zik *et al.* was in a fluidized state and thus there is expected to be a velocity-dependent inertial component to the drag in addition to a
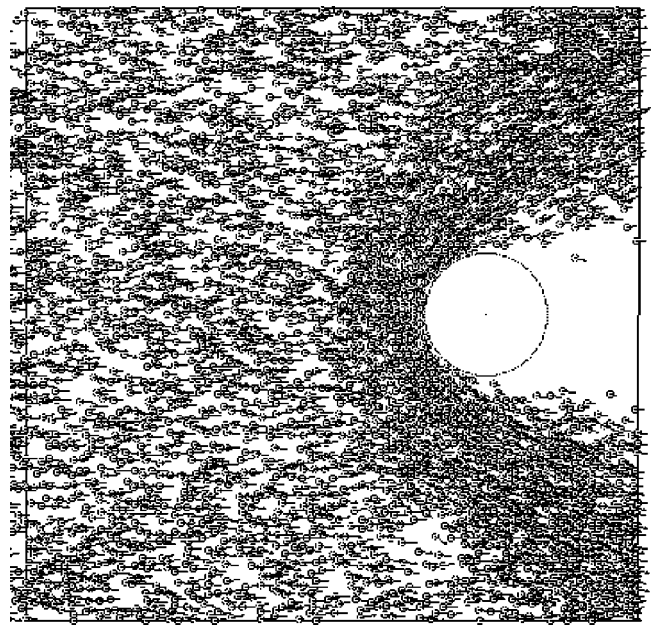

FIG. 1. A snapshot from a soft-particle, periodic boundary simulation with $d=1$ mm, $D=20$ mm, $\rho=2500$ kg/m^3, $U_\infty=1.0$ m/s, $\nu_\infty=0.26$, $T_\infty/U_\infty^2=0.022$, $W=H=100$ mm, $\epsilon_N=0.95$, and $\mu=0$. Velocity vectors are also shown. The flow field is similar to those reported in Buchholtz and Pöschel (Ref. 15).

velocity-independent Coulomb sliding friction component. However, this explanation is not entirely satisfactory since simple analyses and recent computer simulations (to be discussed in Sec. III) indicate that the inertial drag force should be proportional to the square of the flow velocity.

More recently, Buchholtz and Pöschel[15] and Zenit and Karion[16] used discrete element computer simulations to examine the interaction of two-dimensional, dilute granular flows with immersed obstacles. A dilute granular flow is one in which momentum transfer between grains occurs primarily through near-instantaneous, binary collisions. Both groups of researchers found that the drag force on an object, F_d, is proportional to the square of the upstream flow velocity, U_∞, the object's projected diameter, D, and the upstream bulk density, $\rho\nu_\infty$:

$$F_d \propto \rho\nu_\infty U_\infty^2 D, \tag{1}$$

where ρ is the surrounding particle mass density and ν_∞ is the upstream solid fraction. Buchholtz and Pöschel also reported that for slow, but still dilute, flows the drag force is proportional to $U_\infty^{3/2}$ rather than U_∞^2. This trend was not observed in Zenit and Karion's simulations despite using a wide range of velocities.

Both Buchholtz and Pöschel and Zenit and Karion, in addition to Rericha *et al.*,[17] have observed the formation of bow shock waves forming upstream of immersed objects in dilute flows (refer to Fig. 1). These structures are analogous to shock waves found in supersonic flows of gases (see, for example, Shapiro[11]). Indeed, a typical speed of sound in a dilute granular flow[18] is of the order 0.1–1 m/s; thus, most dilute granular flows are in the supersonic regime. Measurements in the experiments of Rericha *et al.* indicated granular Mach numbers of 43 just upstream of the object while Buch-

holtz and Pöschel's simulations had infinite upstream Mach numbers due to a zero upstream granular temperature. The evolution and propagation of a granular shock has also been studied previously by Kamenetsky *et al.*[19] and by Hørlück and Dimon.[20] Relations for the flow conditions across a granular shock in a rapid granular flow have been proposed by Goldshtein *et al.*[21] and by Ocone and Astarita;[22] however, these relations have not been applied to the study of flow conditions around an immersed object.

Despite the previously discussed investigations, there remains a lack of fundamental understanding on the dynamics of granular flows around immersed objects. In particular, the parameters governing the transition from a velocity independent drag force to one that is velocity dependent are poorly understood. This paper examines granular flow around a cylinder in the velocity dependent, dilute flow regime while a companion paper[13] investigates flow in the velocity independent regime.

II. SIMULATION METHODOLOGY

Two-dimensional discrete element (DE), soft- and hard-particle computer simulations were used to investigate the drag force and flow past a cylinder in a dilute granular flow. Details on the soft- and hard-particle DE techniques can be found in a number of papers such as those by Cundall and Strack,[23] Campbell and Brennen,[24] and Walton and Braun.[25] Two different simulation approaches were used to ensure that the results presented here are independent of the simulation details.

A. Soft-particle simulations

The soft-particle simulations consist of a rectangular workspace of width, W, and height, H, containing a fixed cylinder of diameter, D. Moving through the workspace are N cylindrical particles with diameter, d, and mass density, ρ. Two different boundary conditions are considered. The first consists of periodic upper and lower boundaries (Fig. 1). When particles leave the workspace downstream of the cylinder, they are "recycled" to the upstream entrance of the workspace where they are given a random vertical location and random horizontal and vertical velocity components, u and v, respectively, superimposed on a mean horizontal velocity of U_∞ (the mean vertical velocity is zero). In order to avoid large overlaps between particles in this entrance region, particles are given a diameter that is 1% of their final diameter when placed at the upstream boundary. The particles then "grow" to their final diameter within ten particle diameters downstream of the boundary. Several test simulations, where the initial particle size was halved to 0.5% of the final particle diameter and the entrance length was increased to 15 particle diameters, were conducted to verify that this particle recycling algorithm did not affect the simulation results. The second boundary condition consists of a free jet of particles similar to the system investigated by Buchholtz and Pöschel[15] where particles are randomly placed in a rectangular jet of height, H, with a horizontal velocity, U_∞, and no velocity fluctuations.

TABLE I. Baseline soft-particle simulation parameters.

Parameter	Value
Number of particles (periodic boundaries/free jet), N	1000/11111
Particle diameter, d	1 mm
Particle density, ρ	1000 kg/m^3
Cylinder diameter, D	5 mm
Upstream velocity, U_∞	100 mm/s
Workspace width (periodic boundaries only), W	100 mm
Workspace height, H	100 mm
Upstream solid fraction, ν_∞	0.079
Normal coefficient of restitution, ϵ_N	0.95
Particle/particle loading spring constant, k_{Lpp}	1.05×10^4 N/m^2
Particle/cylinder loading spring constant, k_{Lpc}	2.09×10^4 N/m^2
Particle/particle tangential spring constant ratio, k_{Spp}/k_{Npp}	1
Particle/cylinder tangential spring constant ratio, k_{Spc}/k_{Npc}	1
Friction coefficient, μ	0.0
Simulation time step, Δt	2.66×10^{-6} s
Knudsen number, Kn	1.0
Mach number, Ma	∞

The forces acting on particles in the simulation consist only of normal and tangential contact forces; gravity is not considered. The normal contact model consists of a latched, linear spring giving a constant coefficient of restitution as described by Walton and Braun,[25] while the tangential contact model consists of a linear spring in series with a sliding friction element.[23] The time step used in the simulations was determined using the approach described in Corkum and Ting.[26] Halving the time step from the nominal value changed the simulation results by less than 2%. Table I lists the range of parameters used in the baseline soft-particle simulations.

Several quantities were measured in the simulations including the drag force acting on the fixed cylinder and the surrounding particle velocity, solid fraction, and temperature fields. The drag force was found by averaging the horizontal force acting on the fixed cylinder over a long period of time, typically for more time than it takes a particle to travel 1000 cylinder diameters, i.e., $1000D/U_\infty$. These measurements were started after approximately $100D/U_\infty$ in order to eliminate initial transients. A plot of a typical drag force time history is shown in Fig. 2. The surrounding particle fields were found by dividing the workspace into square cells with a side length of at least $2d$, within which the various measured parameters were averaged. A test simulation was conducted in which the averaging cell size was increased from $2d$ to $5d$. The upstream velocity, solid fraction, and temperature results varied by less than 4% from the $2d$ cell size values.

Measurements of the contact duration periods for all particle/particle and particle/cylinder collisions were made in three simulations with upstream solid fractions of 0.15, 0.33, and 0.39 and a normal coefficient of restitution of 0.95. For each of these cases more than 95% of the contacts had a duration equal to that of a binary collision. Hence, these flows have few long-lasting and multiple-particle contacts.
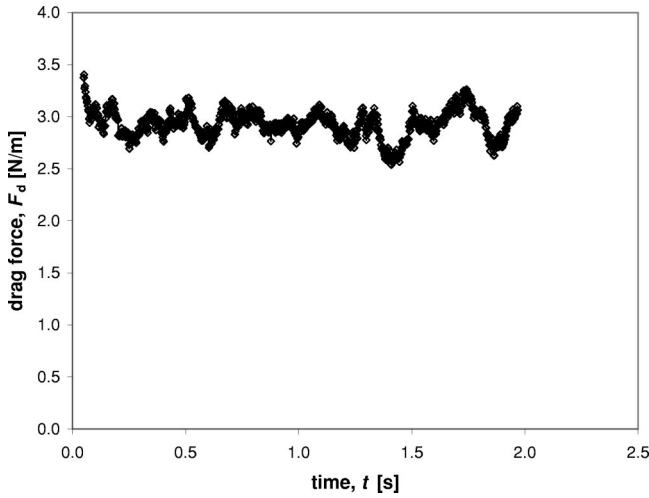
FIG. 2. The drag force acting on the cylinder (per unit depth), F_d, plotted against time, t, from a soft-particle, periodic boundary simulation. The drag force is averaged over a period of 2 ms. The simulation parameters are: $d = 1$ mm, $D = 5$ mm, $\rho = 2500$ kg/m^3, $N = 4000$, $U_\infty = 1.0$ m/s, $\nu_\infty = 0.30$, $T_\infty / U_\infty^2 = 0.024$, $\epsilon_N = 0.9$, and $\mu = 0$.

B. Hard-particle simulations

In order to ensure that the flow measurements are independent of the simulation technique, a hard-particle simulation was also used to investigate dilute granular flow around an immersed cylinder. The hard-particle method is generally more efficient than the soft-particle method for very dilute granular flows where the time between particle collisions is large. It is an event-based algorithm and, hence, is typically applied to granular flows in which only binary, nearly instantaneous collisions occur. The current hard-particle algorithm follows the general approach described by Campbell and Brennen.[24] Additional details can be found in Wassgren et al.[27] Table II lists the baseline parameters used in the hard-particle simulations.

The algorithm is implemented here in two dimensions and without gravity. The workspace consists of a fixed cylinder of diameter, D, immersed in a free jet of circular particles (infinitely long cylinders) of uniform diameter, d, and density, ρ. The workspace geometry is identical to the soft-particle free jet simulation discussed previously. The data

TABLE II. Parameters used in the baseline hard-particle simulation.

Parameter	Value
Number of particles, N	30000
Particle diameter, d	1 mm
Particle density, ρ	1000 kg/m^3
Cylinder diameter, D	5 mm
Upstream velocity, U_∞	100 mm/s
Workspace height, H	100 mm
Upstream solid fraction, ν_∞	0.079
Normal coefficient of restitution, ϵ_N	0.95
Friction coefficient, μ	0
Rolling tangential coefficient of restitution, ϵ_{S0}	-1
Upstream granular temperature, T_∞	0
Knudsen number, Kn	1.0
Mach number, Ma	∞

presented here are collected after the first 100 particle/cylinder impacts and continue for more than 500 impacts with many of the simulations including more than 1000 impacts. Note that the force acting on the cylinder, $\mathbf{F}$, over time T is related to the momentum impulse acting on the cylinder due to particle impacts, $\mathbf{J}$, by

$$\mathbf{F} = \frac{1}{T} \sum_t^{t+T} \mathbf{J}. \tag{2}$$

III. RESULTS AND DISCUSSION

A. Drag force and drag coefficient

First we discuss how the cylinder drag force varies with the flow parameters. It is helpful to consider the following simple two-dimensional analysis of a horizontal stream of *non-interacting* particles colliding with a fixed cylinder. The magnitude of the momentum impulse, $\mathbf{J}$, for an impact between a single particle and the cylinder is given by

$$\mathbf{J} = m(\dot{\mathbf{x}}^+ - \dot{\mathbf{x}}^-) = \rho \frac{\pi d^2}{4}(\dot{\mathbf{x}}^+ - U_\infty \hat{\mathbf{i}}), \tag{3}$$

where m is the mass of the particle per unit depth ($m = \rho(\pi d^2/4)$ for a cylinder), $\dot{\mathbf{x}}^+$ and $\dot{\mathbf{x}}^-$ are the particle velocities immediately after and before contact with the cylinder, respectively, and $\dot{\mathbf{x}}^- = U_\infty \hat{\mathbf{i}}$ is the particle velocity just before impact (equal to the upstream velocity since the reflected and incoming particles do not interact). The particle velocity after the collision is related to the incoming velocity by a normal and tangential coefficient of restitution, ϵ_N and ϵ_S, respectively:

$$\dot{\mathbf{x}}_c^+ \cdot \hat{\mathbf{n}} = -\epsilon_N \dot{\mathbf{x}}_c^- \cdot \hat{\mathbf{n}}, \tag{4}$$

$$\dot{\mathbf{x}}_c^+ \cdot \hat{\mathbf{s}} = -\epsilon_S \dot{\mathbf{x}}_c^- \cdot \hat{\mathbf{s}}, \tag{5}$$

where $\dot{\mathbf{x}}_c$ is the particle surface velocity at the point of contact, $\hat{\mathbf{n}} = -\cos\theta\hat{\mathbf{i}} + \sin\theta\hat{\mathbf{j}}$ and $\hat{\mathbf{s}} = -\sin\theta\hat{\mathbf{i}} - \cos\theta\hat{\mathbf{j}}$ are the unit vectors normal and tangential to the cylinder at the contact point ($\hat{\mathbf{n}} \times \hat{\mathbf{s}} = \hat{\mathbf{k}}$), respectively, and θ is the angle measured with respect to the upstream horizontal to the collision contact point. The particle surface velocity at the contact point is given by

$$\dot{\mathbf{x}}_c = \dot{\mathbf{x}} - \tfrac{1}{2}d\omega\hat{\mathbf{s}}. \tag{6}$$

Note that the incident particles are assumed to have a horizontal velocity $\dot{\mathbf{x}}^- = U_\infty\hat{\mathbf{i}}$ and no rotation, $\omega^- = 0$.

Following the approach described in Walton,[28] the tangential coefficient of restitution is given by

$$\epsilon_S = \begin{cases} -1 + \dfrac{3\mu(1+\epsilon_N)}{\tan\theta} & \text{for}\, |\theta| > \theta_c \\ \epsilon_{S0} & \text{for}\, |\theta| \leq \theta_c \end{cases}, \tag{7}$$

where μ is a sliding friction coefficient and ϵ_{S0} is a constant corresponding to the rolling tangential coefficient of restitution. Note that for a frictionless contact $\epsilon_{S0} = -1$ (or $\mu = 0$), for a pure rolling contact $\epsilon_{S0} = 0$, and for a perfectly elastic tangential rebound $\epsilon_{S0} = 1$. The critical angle θ_c is

$$\tan \theta_c = 3\mu \frac{1+\epsilon_N}{1+\epsilon_{S0}}. \tag{8}$$

The rate at which collisions occur with a small arc length of the cylinder, $d\dot{n}$, is equal to the number flow rate of particles sweeping through the projected vertical width of the arc length:

$$d\dot{n} = \frac{\nu_\infty U_\infty \left(\dfrac{D+d}{2}\right) d\theta}{\dfrac{\pi d^2}{4}}, \tag{9}$$

where ν_∞ is the upstream solid fraction, D is the cylinder diameter, and d is the particle diameter.

The drag force acting on the cylinder is equal to the collision rate multiplied by the horizontal component of the collision impulse integrated over the upstream side of the cylinder (collisions do not occur on the downstream side):

$$F_d = \int_{\theta=-\pi/2}^{\theta=\pi/2} \mathbf{J} \cdot \hat{\mathbf{i}} \, d\dot{n}$$

$$= \frac{1}{2}\rho\nu_\infty U_\infty^2 (D+d)\left[\frac{4}{3}(\epsilon_N+1) + \frac{2}{9}(\epsilon_{S0}+1)\sin^3\theta_c\right]. \tag{10}$$

This analysis demonstrates that for a cylinder of negligible diameter but finite particle diameter, the drag does not approach zero; an observation also noted in the computational study by Buchholtz and Pöschel.[15] In practical terms, this result shows that even a very small probe immersed in a granular flow will have a non-negligible effect on the flow.[15]

Based on Eq. (10) it is natural to define a drag coefficient, C_d, for the cylinder as

$$C_d \equiv \frac{F_d}{\frac{1}{2}\rho\nu_\infty U_\infty^2 (D+d)}. \tag{11}$$

The coefficients of restitution are not included in the drag coefficient in order to maintain similarity with the traditional drag coefficient definition used in fluid mechanics.[29] However, both the cylinder and particle diameter are included in the definition to form an effective cylinder diameter, $D+d$. From Eq. (10) the drag coefficient for a cylinder immersed in a uniform, non-interacting stream of cylindrical particles is expected to be

$$C_d = \frac{4}{3}(\epsilon_N+1) + \frac{2}{9}(\epsilon_{S0}+1)\sin^3\theta_c. \tag{12}$$

Note that the drag coefficient for a cylinder in a free molecular, rarefied gas flow approaches a value of $C_d=8/3$ for very large Mach numbers and specular collisions,[30] the same value predicted by Eq. (12) for frictionless, non-dissipative collisions.

Simulations performed using both soft- and hard-particle simulations indicate that the drag force does indeed increase with the square of the flow velocity and is proportional to both the solid fraction and particle density. The dependence on cylinder and particle diameter has a more complex dependence as will be discussed later. The soft- and hard-particle
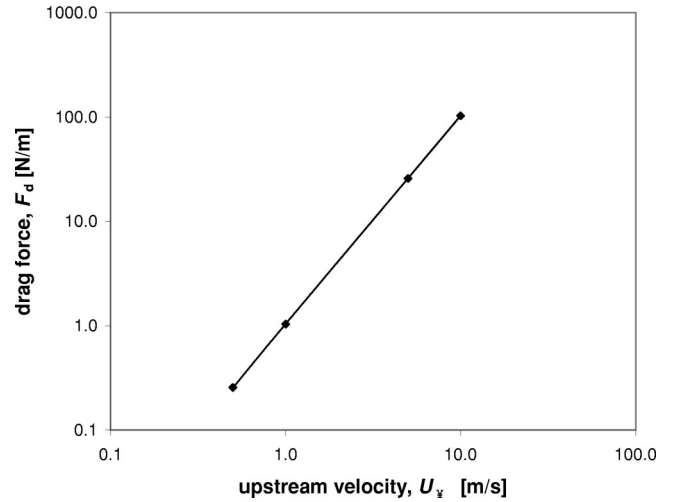

FIG. 3. The drag force acting on the cylinder (per unit depth), F_d, plotted against the upstream velocity, U_∞. Data are for soft-particle, periodic boundary simulations with $d=1$ mm, $D=10$ mm, $\nu_\infty=0.14$, $\rho=1000$ kg/m^3, $\epsilon_N=0.95$, $\mu=0$, and $T_\infty/U_\infty^2=0$. A best fit quadratic trend line to the data is also shown.

simulation techniques gave essentially identical results indicating that the data are independent of the simulation model details. Identical trends were also reported by Buchholtz and Pöschel[15] although they reported that the drag force is proportional to the cylinder diameter. Buchholtz and Pöschel also report that the drag force scales with the velocity to the 3/2 power for small velocities and small cylinder diameters. However, the soft- and hard-particle simulations conducted here do not show such a trend as shown in Fig. 3 where parameters similar to those used in the work by Buchholtz and Pöschel[15] show the $U_\infty^{3/2}$ scaling. (Note that Buchholtz and Pöschel did not report the range of solid fractions for these conditions.) A dimensional analysis of the problem indicates that in order for the drag force to scale with $U_\infty^{3/2}$, some additional time scale must be significant in the problem. Since Buchholtz and Pöschel had no upstream granular temperature in their simulations, the simulation results must have been sensitive to the contact model properties in this regime which have the only remaining time scales in the simulations.

Since a dilute granular flow has similarities with a compressible, rarefied gas flow,[17] it is natural to consider the functional dependence of the drag coefficient on parameters appearing in the analysis of rarefied gas dynamics such as the Mach and Knudsen numbers.

The upstream Mach number, Ma_∞, is defined as

$$\mathrm{Ma}_\infty \equiv \frac{U_\infty}{c_\infty}, \tag{13}$$

where the upstream speed of sound, c_∞, for a granular flow is given by Ocone and Astarita[22] as

$$c_\infty^2 = T_\infty\left[f'(\nu_\infty) + \left(\frac{f(\nu_\infty)}{\nu_\infty}\right)^2\right], \tag{14}$$

where T_∞ is the upstream granular temperature ($T = \frac{1}{2}[\dot{x}'^2 + \dot{y}'^2]$, where $\dot{x}'$ and $\dot{y}'$ are the fluctuating velocities in the x and y directions) and the distribution function, $f(\nu)$, is given by Jenkins and Savage[31] as

$$f(\nu) = \frac{16 - 7\nu}{16(1-\nu)^2}. \tag{15}$$

The upstream Mach number in the present simulations varies from 0.10 to ∞, ranging from subsonic to supersonic flow. An infinite Mach number corresponds to the case where the upstream granular temperature, and hence the speed of sound, is zero.

The Knudsen number is defined as the ratio of the microscopic length scale, here the mean free path of the upstream particles, λ, to the macroscopic length scale, here the cylinder diameter, D:

$$Kn \equiv \frac{\lambda}{D}. \tag{16}$$

In gas dynamics, four flow regimes are defined depending on the Knudsen number.[32] When $Kn < 0.01$ the surrounding flow is considered to be in the "continuum regime" where the fluid can be assumed continuous and there is no-slip between the fluid and boundaries. The "slip regime," where the continuum assumption is still reasonable but slip boundary conditions are used, occurs for $0.01 < Kn < 0.1$. The "free molecular flow" regime, where the continuum assumption breaks down and molecular motion must be considered, occurs when $Kn > 3.0$. A transition regime occurs for $0.1 < Kn < 3.0$ where the mean free path is of the same order as the macroscopic length.

Following the approach given in Liepmann and Roshko,[33] the mean free path of the upstream particles is

$$\lambda = \frac{\pi d}{8 \nu_\infty}. \tag{17}$$

Consequently the Knudsen number for the flow is

$$Kn = \frac{\pi d}{8 \nu_\infty D}. \tag{18}$$

The Knudsen number in the present simulations varies from 0.05 to 10, ranging from the slip to the free molecular flow regime.

The parameters affecting the drag coefficient for rarefied gas flow around a cylinder depend on the flow regime. For slip flow, the drag coefficient depends on both the Reynolds number and Mach number.[34] The drag coefficient for a cylinder in the free molecular flow regime decreases approximately inversely with the Mach number.[30] with $C_d \to 8/3$ as $Ma_\infty \to \infty$, identical to what is predicted by Eq. (12) for frictionless, non-dissipative collisions.

The drag coefficient is first plotted as a function of Mach number for Knudsen numbers of $Kn \approx 0.56$ and $Kn \approx 2.3$ (Fig. 4). The drag coefficient is insensitive to the Mach number when $Ma_\infty > 1$. However, when $Ma_\infty < 1$, the drag coefficient increases rapidly with decreasing Mach number. Note that the granular temperature of the flow decays over time due to particle collisions so that without an external source
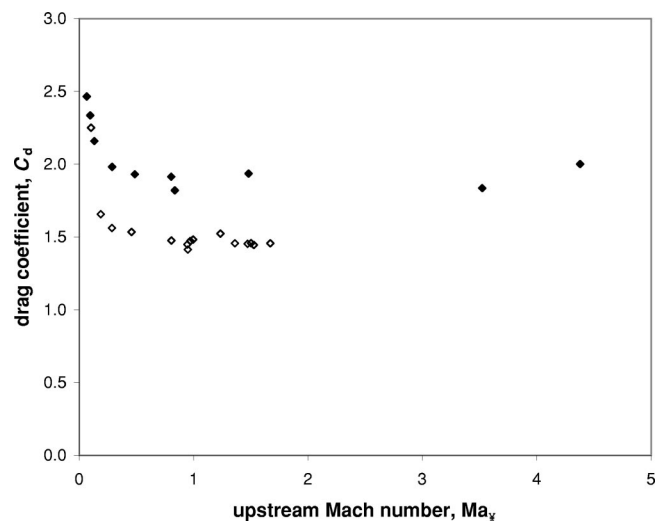

FIG. 4. The drag coefficient, C_d, plotted against the upstream Mach number, Ma_∞, for $Kn = 0.6$ ($\diamond$) and $Kn = 2.3$ ($\blacklozenge$). The data are from soft-particle, periodic boundary simulations.

of fluctuation energy, the flow will tend toward an infinite Mach number. The soft-particle, periodic boundary simulations were used to investigate the Mach number dependence since there is only a slight decay in the initial granular temperature from the upstream boundary to the cylinder.

Figure 5 plots the drag coefficient against Knudsen number for infinite Mach numbers so that the subsonic Mach number dependence is avoided. The data follow a clear trend with the drag coefficient increasing with increasing Knudsen number and appearing to approach the value predicted for the large Kn and Ma limit [Eq. (12)]. The data shown in the figure were calculated using various combinations of cylin-
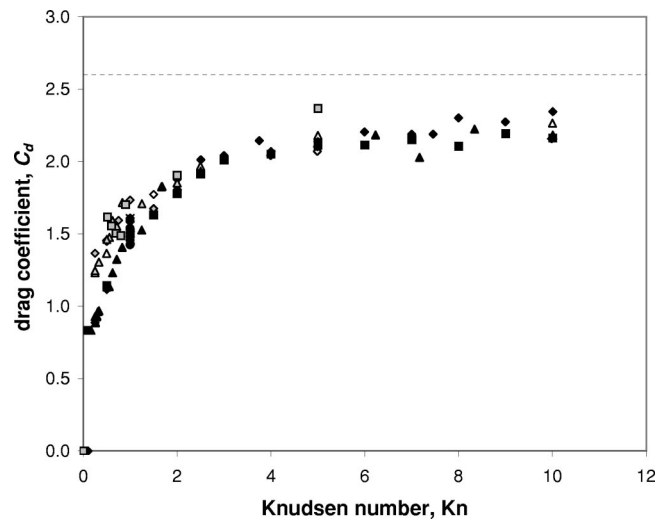

FIG. 5. The drag coefficient, C_d, plotted against the Knudsen number, Kn, for infinite Mach numbers. $\triangle$ = variations in the cylinder diameter, D; $\diamond$ = variations in the upstream solid fraction, ν_∞; $\square$ = variations in the particle diameter d; $\times$ = variations in the particle density, ρ; $\bigcirc$ = variations in the upstream velocity, U_∞. The black, gray, and white symbols are for the soft-particle periodic boundary, soft-particle free jet, and hard-particle free jet simulations, respectively. The baseline simulation parameters are summarized in Tables I and II. The dashed line corresponds to the prediction of Eq. (12).
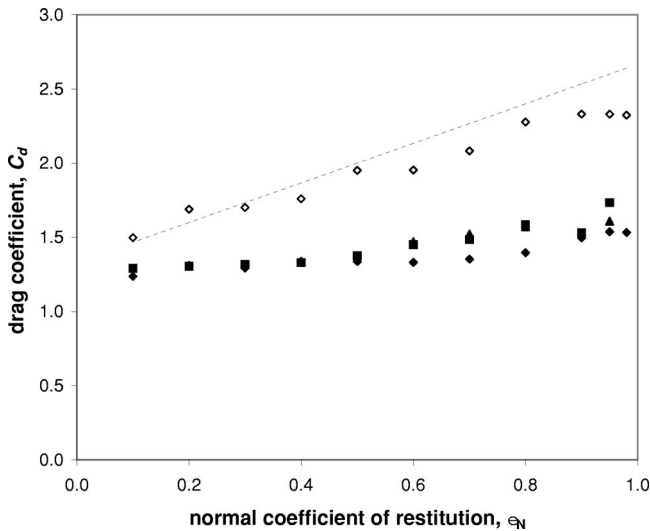
FIG. 6. The drag coefficient, C_d, plotted against the normal coefficient of restitution, ϵ_N. $\triangle$=soft-particle, periodic boundaries (data only for $0.6 \leqslant \epsilon_N \leqslant 0.95$, Kn=1); $\square$=soft-particle, free jet (data only for Kn=1); $\diamond$=hard-particle, free jet. The closed and open symbols are for Kn=1 and Kn=10, respectively. Note that the normal coefficient of restitution is the same between the particles and the particles and the cylinder. The remainder of the simulation parameters are given in Tables I and II. The dashed line corresponds to the prediction of Eq. (12).

FIG. 8. The drag coefficient, C_d, plotted against the domain height, H, normalized by the effective cylinder diameter, $(D+d)$, for various system aspect ratios, H/W ($\square$=H/W=0.5; $\blacklozenge$=H/W=1.0; $\triangle$=H/W=2.0). The center of the cylinder is located at a distance of $0.75W$ from the upstream boundary. The data are from soft-particle, periodic boundary simulations with D=5 mm, d=1 mm, ϵ_N=0.95, μ=0, Kn=0.35, and infinite Mach number. The remainder of the simulation parameters are given in Table I.

der diameter, particle diameter, and solid fraction to produce a range of Knudsen numbers. The figure also includes data at Kn=1 for simulations using different upstream velocities and particle densities.

The effect of the normal coefficient of restitution on the drag coefficient is shown in Fig. 6 for a flow with no upstream granular temperature (infinite Mach number) and frictionless particles. Note that the normal coefficient of restitu-
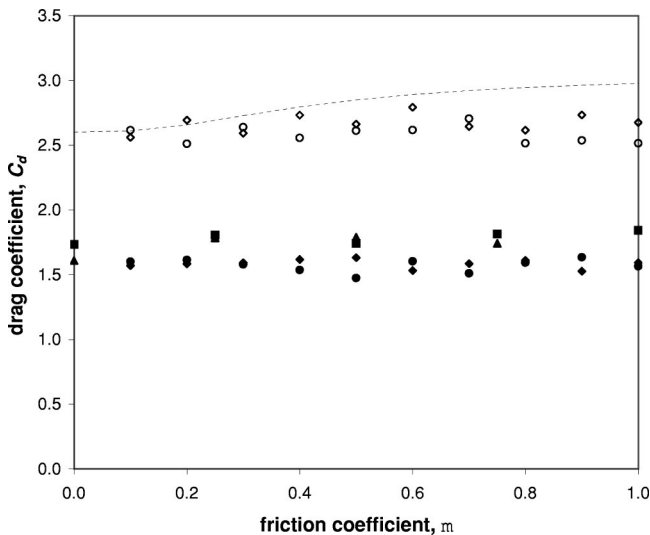
tion was the same for particle/particle and particle/cylinder collisions. At a Knudsen number of 10 the drag coefficient closely follows the trend predicted by Eq. (12). However, for Kn=1 the drag coefficient is less sensitive to the normal coefficient of restitution, especially for small values of ϵ_N. The discrepancy with the analysis occurs because the analysis assumes that reflected particles do not interact with incident particles, an assumption that is not satisfied for the given flow conditions. This assumption has even greater error at small ϵ_N since reflected particles remain in the vicinity

FIG. 7. The drag coefficient, C_d, plotted against the friction coefficient, μ. $\triangle$=soft-particle, periodic boundaries (data only for Kn=1); $\square$=soft-particle, free jet (data only for Kn=1); $\diamond$=hard-particle, free jet with ϵ_{S0}=1.0; $\bigcirc$=hard-particle, free jet with ϵ_{S0}=0.35. The closed and open symbols are for Kn=1 and Kn=10, respectively. Note that the friction coefficient is the same between the particles and the particles and the cylinder. The dashed line corresponds to the prediction of Eq. (12). The remainder of the simulation parameters is given in Tables I and II.
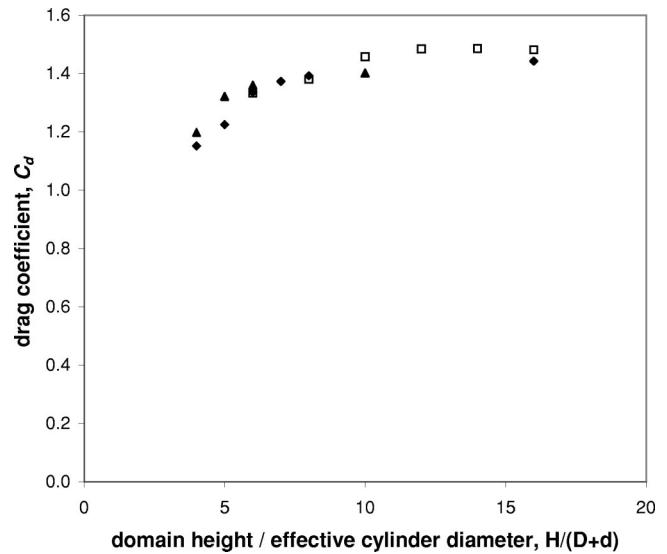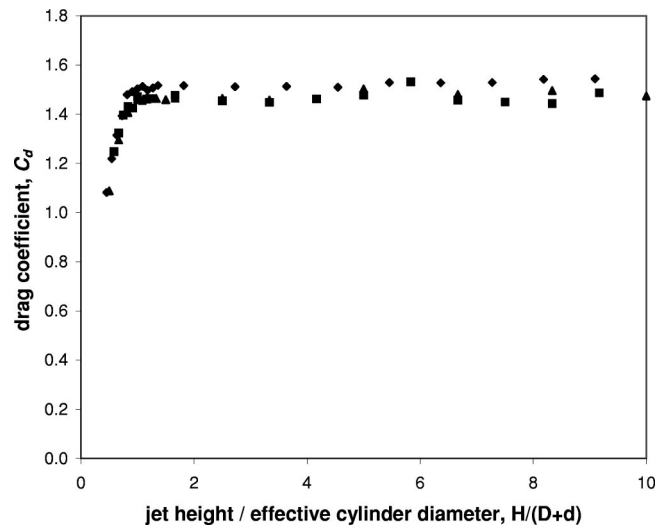

FIG. 9. The drag coefficient, C_d, plotted against the jet height, H, normalized by the effective cylinder diameter, $(D+d)$, for the hard-particle, free jet simulations. $\blacktriangle$=(D,d)=(5,1) mm; $\blacklozenge$=(D,d)=(10,1) mm; $\blacksquare$=(D,d)=(10,2) mm. The remainder of the simulation parameters is given in Table II.
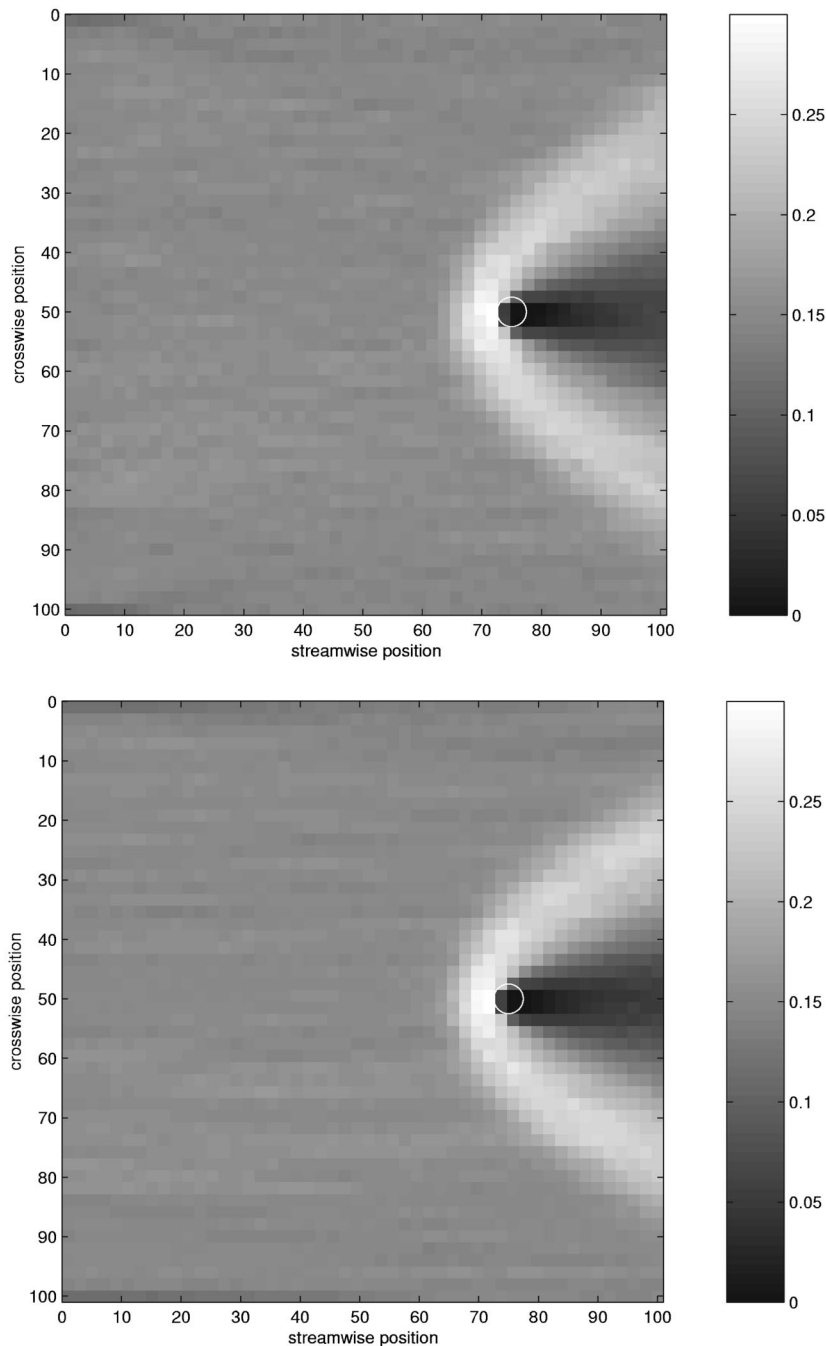
FIG. 10. The solid fraction field around the cylinder for (top) $Ma_\infty = 0.81$ and (bottom) $Ma_\infty = 1.78$. The remaining parameters are $Kn = 0.52$, $\nu_\infty = 0.15$, $D/d = 5$, $W/d = H/d = 100$, $\mu = 0$, and $\epsilon = 0.95$. The center of the cylinder is located at $(x/W, y/H) = (0.75, 0.50)$. Note that the "particle growth" region is located adjacent to the upstream boundary.

of the cylinder and interact more frequently with the incoming stream. Figure 6 also shows that the soft- and hard-particle free jet simulations give nearly identical results at small ϵ_N, but give the largest discrepancies at the largest ϵ_N. This trend is somewhat counter-intuitive. It is reasonable to expect that the difference between the drag coefficients will increase as ϵ_N decreases since the average collision contact duration in the soft-particle simulations increases linearly with decreasing ϵ_N while in the hard-particle simulations the contact duration is instantaneous, by definition. The cause for the observed simulation trend remains unclear.

The simulations were also used to investigate the drag coefficient dependence on the friction coefficient, μ, for flows with no upstream granular temperature and a constant

normal coefficient of restitution of $\epsilon_N = 0.95$. The particle/particle and particle/cylinder friction coefficients were equal in all of the simulations. The tangential spring constant remained constant in all of the soft-particle simulations (the value is given in Table I) while the hard particle simulations used two different values of the rolling tangential coefficient of restitution: $\epsilon_{S0} = 0.35$ and $\epsilon_{S0} = 1$. Note that Drake[35] found experimentally that $\epsilon_{S0} \approx 0.35$ for plastic sphere impacts. Equation (12) predicts that the drag coefficient with friction at the large Knudsen and Mach number limit will be, at most, only 17% greater than the drag coefficient without friction. Figure 7 demonstrates that the drag coefficient does indeed have only a weak dependence on the friction coefficient for both $Kn = 10$ and $Kn = 1$. Furthermore, there is little differ-
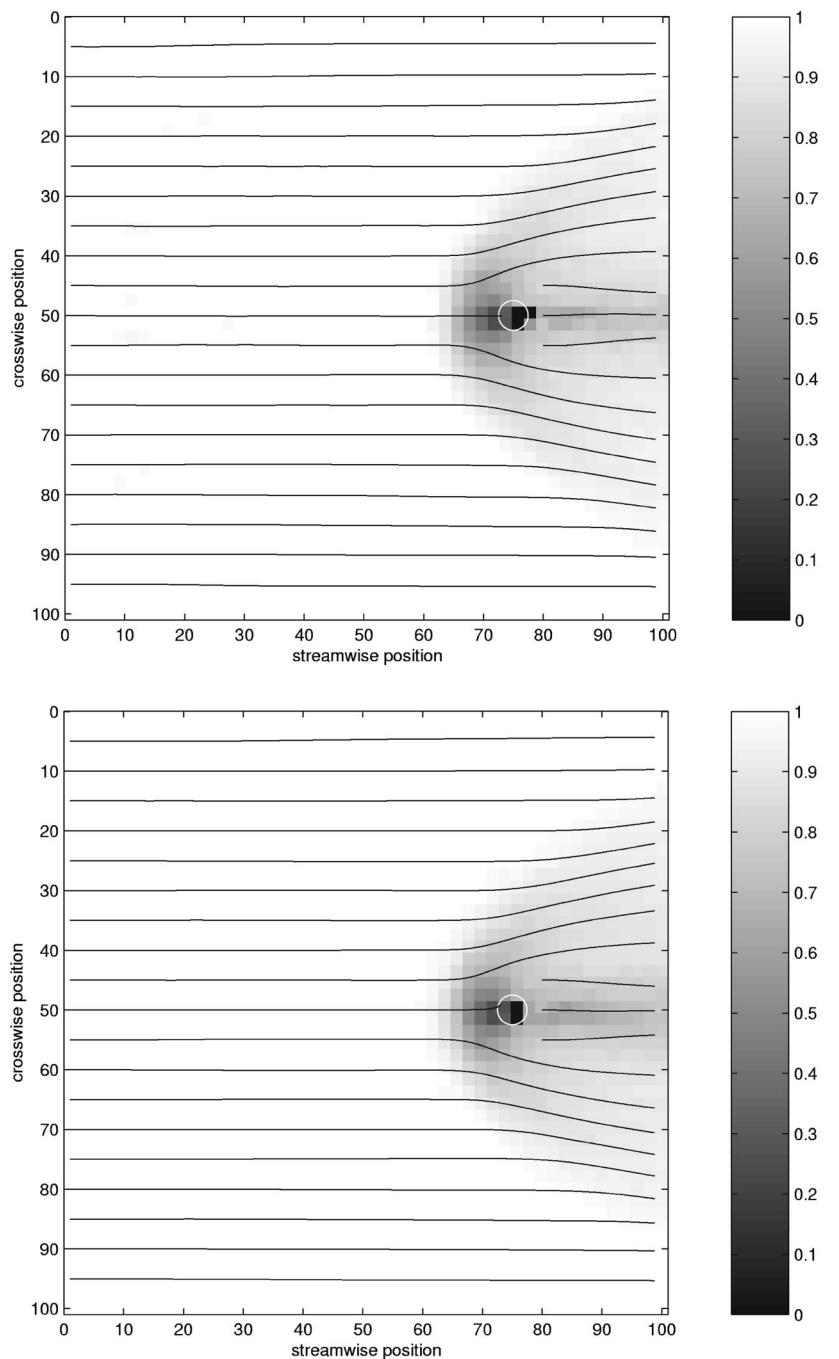
FIG. 11. The dimensionless velocity field, U/U_∞, around the cylinder for the flow conditions given in Fig. 10. Streamlines are superimposed.

ence between the $\epsilon_{S0}=0.35$ and $\epsilon_{S0}=1.0$ cases in the hard-particle simulations. The analysis used to derive Eq. (12) indicates that the weak tangential coefficient of restitution dependence is due to particle rotation over the cylinder surface for large friction coefficients.

The effect of the workspace dimensions, W and H, was also investigated. Figure 8 plots the drag coefficient as a function of the workspace height normalized by the effective cylinder diameter, $H/(D+d)$, for various domain aspect ratios, H/W. The cylinder was located along the centerline of the workspace a distance $0.75W$ from the upstream periodic boundary. The data indicate that, for the conditions investigated, the drag coefficient increases with increasing domain height and approaches a nearly constant value for $H/(D$

$+d)>10$. The trend appears independent of the domain aspect ratio H/W. Simulation animations show that when the domain aspect ratio is too small, the bow shock structures that form in front of the cylinder (to be discussed in Sec. III B) interact across the periodic boundaries. For the hard-particle free jet simulations the drag coefficient remains unaffected by the dimensionless jet width, $H/(D+d)$, for $H/(D+d)>1$ as shown in Fig. 9. The effect of jet width was not studied for the soft-particle free jet simulations.

B. Flow fields

In addition to the drag force acting on the cylinder, the solid fraction, velocity, and granular temperature fields
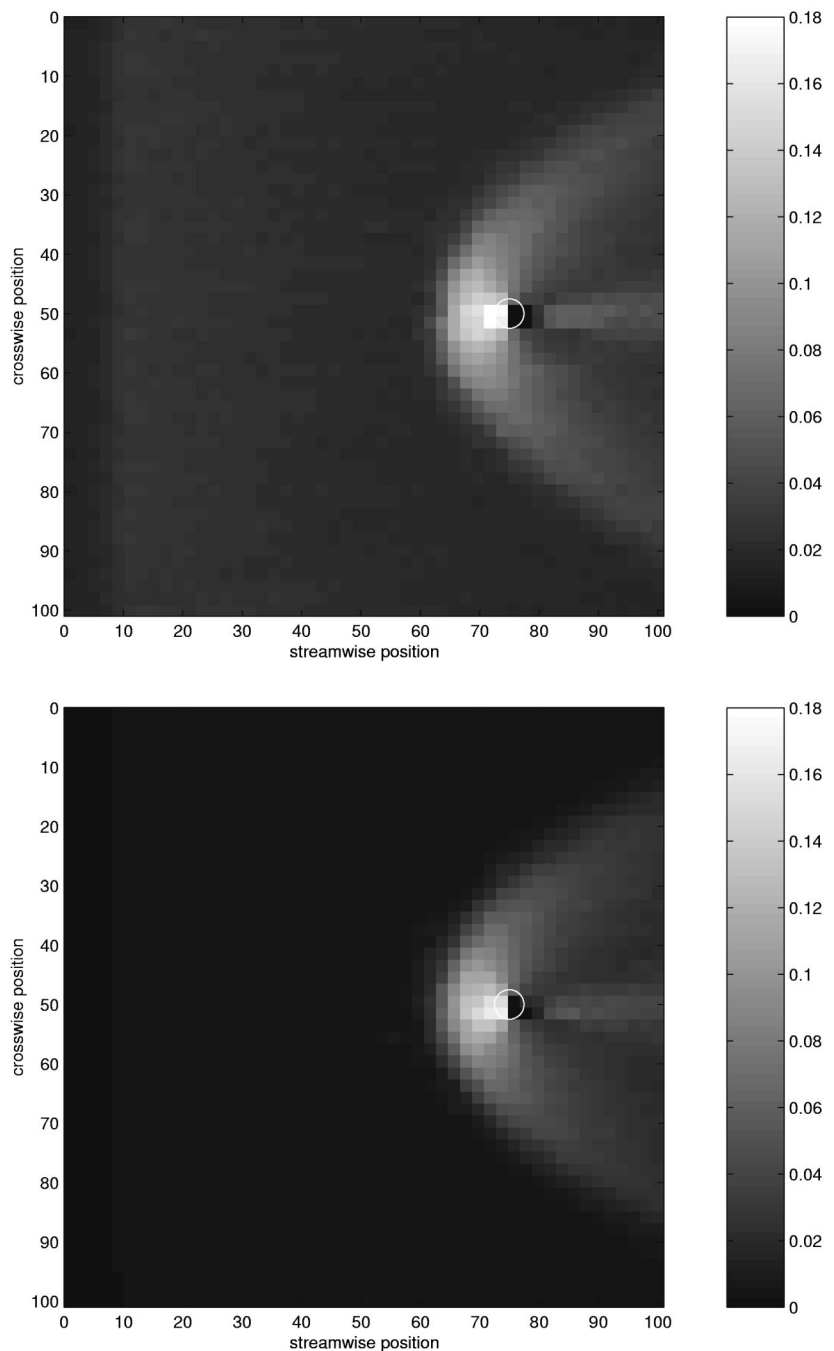
FIG. 12. The dimensionless granular temperature field, T/U_∞^2, around the cylinder for the flow conditions given in Fig. 10.

around the cylinder were also measured in the simulations. The results discussed in the following were determined using the soft-particle simulations.

A plot of the solid fraction field is shown in Fig. 10 for two flows with Kn=0.52 and Ma_∞=0.81 and Ma_∞=1.78 (the remainder of the parameters are given in the figure caption). Bow shock structures are observed upstream of the cylinder with expansion fan regions observed behind the cylinders. Directly behind the cylinders is a wake region containing very few particles. Similar shock and expansion structures have been observed in the dilute granular flow simulations of Buchholtz and Pöschel[15] and the experiments of Rericha et al.[17] and Amarouchene et al.[36]

The corresponding velocity and granular temperature

fields are shown in Figs. 11 and 12, respectively. A region of low velocity, high temperature particles occurs behind the shock wave in front of the cylinders; however, a stagnant region as described by Amarouchene et al.[36] is not observed. This discrepancy is most likely due to the use of frictionless particles in the simulations and the low simulation upstream solid fractions (Amarouchene et al. do not report the solid fractions in their experiments). Note that in most dilute granular flows, the solid fraction and granular temperature are typically inversely dependent.[37] However, across the shocks observed here both the solid fraction and granular temperature increase. A "tail" of moderate temperature is observed in the wake region behind the cylinder. This region
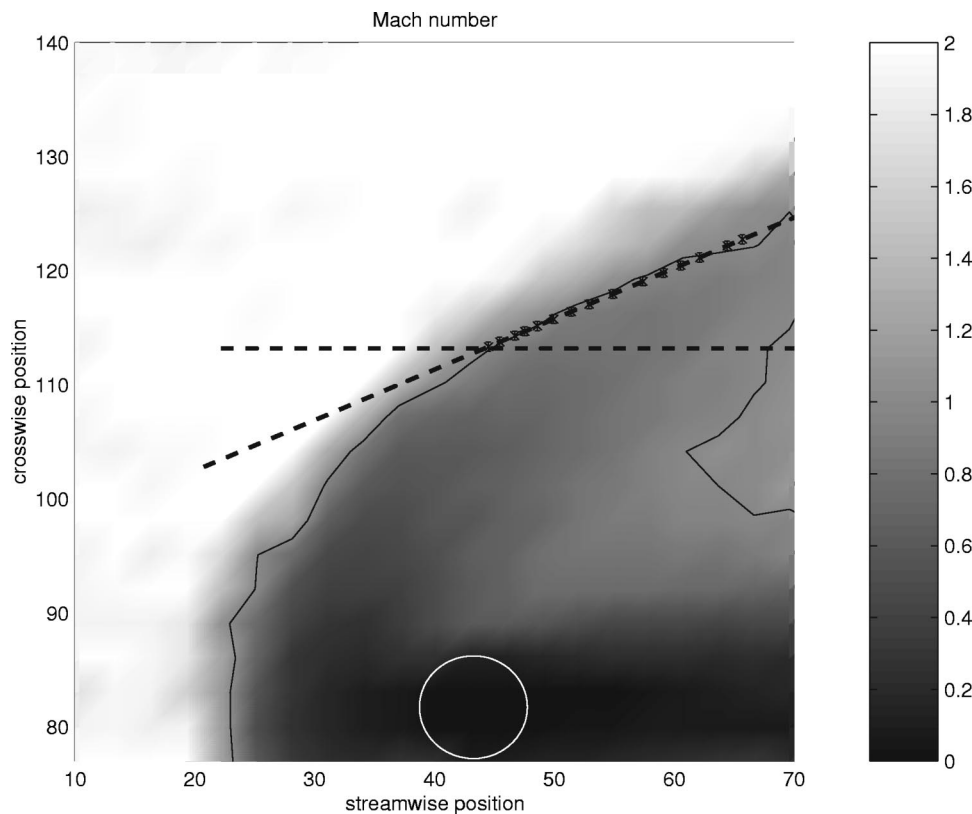
Mach number

FIG. 13. The Mach number field around the cylinder for $Ma_\infty = 1.99$ and $\nu_\infty = 0.21$. Only the upper half of the domain is shown for clarity. The inclined line is a linear fit to the iso-Mach number line ($Ma = 1$) and is used to calculate the shock angle, β. Measurements across the shock (Fig. 14) are taken along the horizontal line.

contains few particles so that fluctuations in the particle velocities can be significant.

Surprisingly, the solid fraction, velocity, and temperature fields look similar for both flows despite the Mach number difference. The angle of the "bow shock" with respect to the horizontal appears to be roughly equal for both Mach numbers. The only significant observable difference between the two flows is that the temperature downstream of the bow shock decays more rapidly for $Ma_\infty = 1.78$ than for $Ma_\infty = 0.81$.

A typical Mach number field is shown in Fig. 13 for an upstream Mach number, Knudsen number, and solid fraction of 1.99, 0.18, and 0.21, respectively. In contrast to typical supersonic gas dynamics flows, the shock structure cannot be considered as a discontinuity in the flow and instead changes in flow properties occur over a distance comparable to the cylinder radius.

The angle the bow shock makes with respect to the upstream flow far from the cylinder was measured for four flows with $(Ma_\infty, \nu_\infty) = (1.99, 0.10), (1.07, 0.10), (1.96, 0.21)$ and $(1.34, 0.21)$. The shock angle, β, was determined by fitting a line to the $Ma = 1$ iso-Mach number line as shown in Fig. 13. The shock angle is remarkably insensitive to the upstream flow Mach number, a situation very different from typical compressible fluid flows. The bow shock angle decreases from $29° \pm 1°$ to $26° \pm 1.5°$ for an increase in Mach number from $Ma_\infty = 1.34$ to $Ma_\infty = 1.96$. For an identical increase in Mach number in a compressible air flow, the oblique shock angle would decrease by, at the minimum, $18°$.

Measurements of the flow Mach number, solid fraction, granular temperature, and velocity deflection angle were made along a horizontal line crossing the bow shock (refer to Fig. 13) and are plotted in Fig. 14. The velocity deflection angle is defined as the angle by which the average velocity vector changes across the shock wave. The flow properties change over a distance of approximately five to ten particle diameters, comparable to the cylinder diameter of $D/d = 10$. Downstream of the shock, the solid fraction and velocity deflection angle remain nearly constant; however, the granular temperature decreases and, as a result, the Mach number increases. The decrease in granular temperature occurs presumably due to the energy dissipated in particle collisions downstream of the shock. For all of the cases shown, the Mach number immediately downstream of the shock is subsonic. Because the normal velocity decreases while the tangential velocity remains constant, a compressible fluid turns toward the shock wave through an angle θ. Note that for compressible gas flows, the velocity deflection angle, θ, can be determined if the upstream Mach number and shock angle, β, are known (see, for example, Liepmann and Roshko[33]). In air with $Ma_\infty = 1.96$ and $\theta = 10°$, the oblique wave angle is $\beta = 40°$, a value considerably different than the $\beta = 29°$ measured in the granular flow for $Ma_\infty = 1.96$, $\nu_\infty = 0.21$, and $\theta \approx 10°$. The velocity deflection angle for $Ma_\infty = 1.34$ and $\nu_\infty = 0.21$ is also $\theta \approx 10°$. A solution for the oblique shock wave angle does not exist for an identical Mach number and velocity deflection angle for air, however.

IV. CONCLUSIONS

The present studies indicate that a cylinder immersed in a dilute granular flow has many similarities with rarefied gas
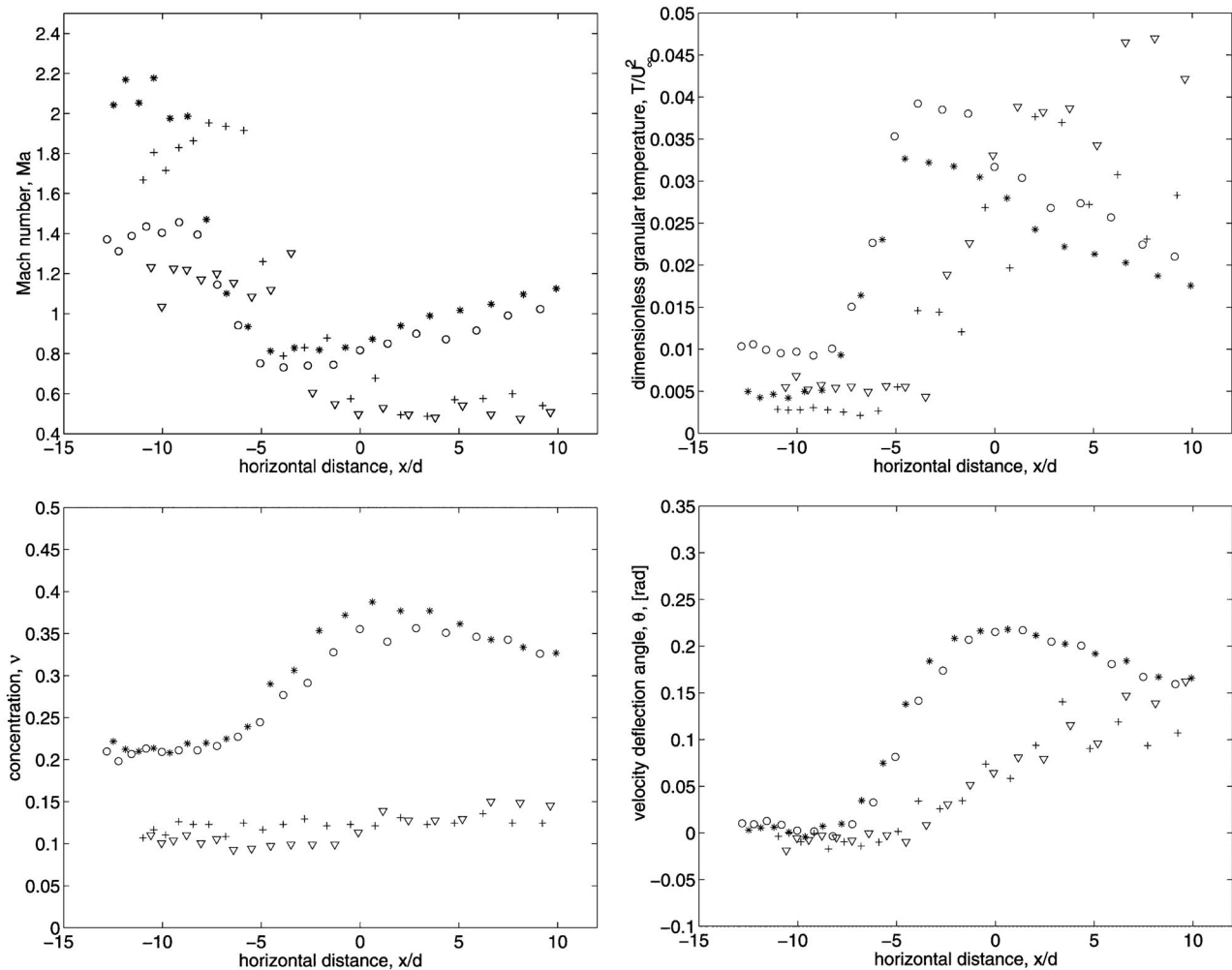
FIG. 14. Flow properties along a horizontal line crossing a granular shock wave. The location of the line is shown in Fig. 13. The location $x/d = 0$ corresponds to the horizontal position of the cylinder center. The symbols correspond to: $(+, \nu_\infty = 0.10, \mathrm{Ma}_\infty = 1.99, \mathrm{Kn} = 0.37)$, $(\nabla, 0.10, 1.07, 0.39)$, $(\bigcirc, 0.21, 1.34, 0.18)$, and $(*, 0.21, 1.96, 0.18)$.

flow. The drag coefficient for the cylinder (defined using the effective cylinder diameter, $D + d$, and the upstream bulk density, $\rho \nu_\infty$) depends strongly on the flow Knudsen number with a secondary dependence on the upstream Mach number. The drag coefficient decreases with decreasing normal coefficient of restitution and is relatively insensitive to the friction coefficient. Shock and expansion fan structures, similar to those observed in gas dynamics, are also observed in these dilute granular flows. These structures appear to vary little with the granular Mach number. Granular kinetic theories (see, for example, Jenkins and Savage[31]) are applicable in this flow regime and should provide greater insight into the flow dynamics.

A companion article by Chehata et al.[13] investigates granular flow around a cylinder immersed in a dense, frictional granular flow. In these experiments the drag coefficient is independent of the flow velocity. Future studies should investigate the drag force transition from the velocity squared dependence for dilute granular flows to the velocity independence for dense granular flows.

[1] *Principles of Powder Technology,* edited by M.J. Rhodes (Wiley, New York, 1990).
[2] U. Tüzün and R.M. Nedderman, "Gravity flow of granular materials round obstacles. I. Investigation of the effects of inserts on flow patterns inside a silo," Chem. Eng. Sci. **40**, 325 (1985).
[3] J. Hernandez-Cordero, R. Zenit, E. Geffroy, B. Mena, and R.R. Huilgol, "Experiments on granular flow in a hexagonal silo: A design that minimizes dynamic stresses," Korea-Australia J. Rheol. **12**, 269 (2000).
[4] I.K.J. Melzer, "Soil exploration from the air," J. Indian Nat. Soc. of Soil Mech. and Found. Eng. **9**, 363 (1970).
[5] J.C. Pearce and R.H. Sabersky, "Thermal wake and separation point for the flow of a granular medium around a heated cylinder," Lett. Heat Mass Transfer **4**, 1 (1977).
[6] A. Rosato, K.J. Strandburg, F. Prinz, and R.H. Swendsen, "Why the Brazil nuts are on top: Size segregation of particulate matter by shaking," Phys. Rev. Lett. **58**, 1038 (1987).

[7] K. Wieghardt, "Forces in granular flow," Mech. Res. Commun. **1**, 3 (1974).

[8] R. Albert, M.A. Pfeifer, A.-L. Barabási, and P. Schiffer, "Slow drag in a granular medium," Phys. Rev. Lett. **82**, 205 (1999).

[9] T.D. Atkinson, J.C. Butcher, M.J. Izard, and R.M. Nedderman, "The forces on obstacles suspended in flowing granular materials," Chem. Eng. Sci. **38**, 91 (1983).

[10] R.M. Nedderman, *Statics and Kinematics of Granular Materials* (Cambridge University Press, Cambridge, 1992).

[11] A.H. Shapiro, *The Dynamics and Thermodynamics of Compressible Fluid Flow* (Wiley, New York, 1953).

[12] U. Tüzün and R.M. Nedderman, "Gravity flow of granular materials round obstacles—II," Chem. Eng. Sci. **40**, 337 (1985).

[13] D. Chehata, R. Zenit, and C.R. Wassgren, "Dense granular flow around a cylinder," Phys. Fluids **15**, 1622 (2003).

[14] O. Zik, J. Stavans, and Y. Rabin, "Mobility of a sphere in vibrated granular media," Europhys. Lett. **17**, 315 (1992).

[15] V. Buchholtz and T. Pöschel, "Interaction of a granular stream with an obstacle," Granular Matter **1**, 33 (1998).

[16] R. Zenit and A. Karion, "Granular flow around a cylinder," Proceedings of the 2000 AIChE Annual Fall Meeting, Los Angeles, CA, 2000.

[17] E.C. Rericha, C. Bizon, M.D. Shattuck, and H.L. Swinney, "Shocks in supersonic sand," Phys. Rev. Lett. **88**, 014302 (2002).

[18] S.B. Savage, "Streaming motions in a bed of vibrationally fluidized dry granular material," J. Fluid Mech. **194**, 457 (1988).

[19] V. Kamenetsky, A. Goldshtein, M. Shapiro, and D. Degani, "Evolution of a shock wave in a granular gas," Phys. Fluids **12**, 3036 (2000).

[20] S. Hørlück and P. Dimon, "Grain dynamics in a two-dimensional granular flow," Phys. Rev. E **63**, 031301 (2001).

[21] A. Goldshtein, M. Shapiro, L. Moldavsky, and M. Fichman, "Mechanics of collisional motion of granular materials. Part 2. Wave propagation through vibrofluidized granular layers," J. Fluid Mech. **287**, 349 (1995).

[22] R. Ocone and G. Astarita, "Compression and rarefaction waves in granular flow," Powder Technol. **82**, 231 (1995).

[23] P.A. Cundall and O.D.L. Strack, "A discrete numerical model for granular assemblies," Geotechnique **29**, 47 (1979).

[24] C.S. Campbell and C.E. Brennen, "Chute flows of granular material: Some computer simulations," Trans. ASME, J. Appl. Mech. **52**, 172 (1985).

[25] O.R. Walton and R.L. Braun, "Viscosity, granular-temperature, and stress calculations for shearing assemblies of inelastic, frictional disks," J. Rheol. **30**, 949 (1986).

[26] B.T. Corkum and J.M. Ting, "The discrete element method in geotechnical engineering," Publication 86-11, University of Toronto, Toronto, 1986.

[27] C. Wassgren, J.A. Cordova, and R. Zenit, "The unsteady drag force on a cylinder immersed in a dilute granular flow," Proceedings of the Sixth Conference on Computer Simulation and Industrial Applications, edited by S. Raczynski, Tijuana, Mexico, 2003.

[28] O.R. Walton, "Numerical simulation of inelastic, frictional particle–particle interactions," in *Particulate Two-Phase Flow*, edited by M.C. Roco (Butterworth-Heinemann, Stoneham, MA, 1993).

[29] R.W. Fox and A.M. McDonald, *Introduction to Fluid Mechanics* (Wiley, New York, 1999).

[30] S.A. Schaaf and P.L. Chambré, *Flow of Rarefied Gases* (Princeton University Press, Princeton, NJ, 1961).

[31] J.T. Jenkins and S.B. Savage, "A theory for the rapid flow of identical, smooth, nearly elastic, spherical particles," J. Fluid Mech. **130**, 187 (1983).

[32] M.J. Zucrow and J.D. Hoffman, *Gas Dynamics* (Wiley, New York, 1976), Vol. I.

[33] H.W. Liepmann and A. Roshko, *Elements of Gasdynamics* (Wiley, New York, 1957).

[34] H.S. Tsien, "Superaerodynamics, mechanics of rarefied gases," J. Aeronaut. Sci. **13**, 653 (1946).

[35] T.G. Drake, "Experimental flows of granular materials," Ph.D. dissertation, UCLA, 1988.

[36] Y. Amarouchene, J.F. Boudet, and H. Kellay, "Dynamic sand dunes," Phys. Rev. Lett. **86**, 4286 (2001).

[37] C.S. Campbell, "Rapid granular flows," Annu. Rev. Fluid Mech. **22**, 57 (1990).